# Acceleration of Ferromagnetic Resonance (FMR) Measurements by Bayesian Experimental Design

D. Huang,[1,2] X. Wang,[2] and D. B. Gopman[1, *]

[1]*Materials Science and Engineering Division, National Institute of Standards and Technology, Gaithersburg, Maryland, 20899, USA*

[2]*Department of Mechanical Engineering, University of Minnesota, Minneapolis, Minnesota, 55455, USA*

Ferromagnetic resonance (FMR) is a broadly used dynamical measurement used to characterize a wide range of magnetic materials. Applied research and development on magnetic thin film materials is growing rapidly alongside a growing commercial appetite for magnetic memory and computing technologies. The ability to execute high-quality, fast FMR surveys of magnetic thin films is needed to meet the demanding throughput associated with rapid materials exploration and quality control. Here, we implement an optimal Bayesian experimental design software developed by McMichael *et al*. [1] in a vector network analyzer-FMR setup to demonstrate an unexplored opportunity to accelerate FMR measurements. A systematic comparison is made between the optimal Bayesian measurement and the conventional measurement. Reduced uncertainties in linewidth and resonance frequency ranging from 40 % to 60 % are achieved with the Bayesian implementation for the same measurement duration. As the optimal Bayesian approach only decreases random errors, we evaluate how large systematic errors may limit the full advantage of the optimal Bayesian approach. This approach can be used to deliver gains in measurement speed by a factor of three or more and as a software add-on, has the flexibility to be added on to any FMR measurement system to accelerate materials discovery and quality control measurements, alike.

* Author to whom correspondence should be addressed: daniel.gopman@nist.gov

## I. INTRODUCTION

Ultrathin magnetic films and multilayers are widely used in data storage [2,3] and are gaining traction in next-generation memory [4-6] and computing [7,8] devices. The performance of these devices relies heavily on the magnetic properties of the constituent materials, including the magnetic anisotropy for data retention and Gilbert damping for magnetic relaxation and energy dissipation [9]. Therefore, materials engineering becomes pivotal and demands high-throughput methods for materials characterization to advance structure-processing-function relationships in these technologically-relevant material classes.

Ferromagnetic resonance spectroscopy (FMR) is one of the most widely-adopted measurement techniques used to evaluate the intrinsic magnetic properties of materials. Typically carried out with a magnetically saturated specimen, FMR informs on key intrinsic properties, such as effective magnetization/effective magnetic anisotropy fields [10], gyromagnetic ratio [11], damping [12], and exchange constant [13]. The earliest FMR investigations were typically carried out in radio-frequency (*rf*) cavity environments with a fixed excitation frequency and under a swept external magnetic field [14,15]. Later studies replaced the cavity geometry with stripline and coplanar transmission lines, introducing the broadband FMR approach used today to track the frequency-field dispersion across a wide range of frequencies, simplifying the characterization of key magnetic properties like the Gilbert damping constant and the spectroscopic *g*-factor [12,16-18]. Broadband FMR can be implemented in a field-modulation scheme, with a dedicated microwave generator, a diode detector, and a lock-in amplifier paired with modulation coils [19]. This scheme usually is carried out in a field-swept mode at fixed *rf* frequency, minimizing the influence of the complex frequency response of a transmission line loaded by a magnetic thin film sample and enabling FMR detection of magnetic thin film specimens only a few monolayers thick [20,21]. Another alternative for broadband FMR uses a vector network analyzer (VNA) to both generate the *rf* stimulus and detect the complex transmission and reflection coefficients of the device under test – in this case, the loaded transmission line (VNA-FMR) [22]. In addition to field-swept observations at fixed *rf* frequency, VNA-FMR also supports a frequency-swept mode, which is especially useful for observing FMR under specific magnetic fields within a specimen's major (or minor) magnetic hysteresis loop [19,23,24]. However, a conventional VNA-FMR setup does not have field modulation and consequently the FMR signal can be overwhelmed by a larger low-frequency noise background. Worse still is the case of frequency-swept scans, for which a non-magnetic background overwhelms the FMR signal [19,25]. Recently, a modification on VNA-FMR by adding field modulation was introduced to take advantage of the narrow noise bandwidth associated with frequency scans and the background rejection of non-magnetic contributions derived by subtracting two frequency scans under different external magnetic fields

[25]. This so-called field-differential VNA-FMR approach can enhance the signal-to-noise ratio (SNR) and suppress frequency-dependent background [25].

Conventional execution of FMR measurements is informed by existing, but typical knowledge about specimens. For example, an experimenter often knows the form of the resonance frequency-field relationship, depending on the projection of an external magnetic field along a symmetry direction and the shape of the specimen. In the special case of a thin-film sample, the Kittel equation presents simplified analytical expressions for the dispersion under applied fields either perpendicular to the film plane or within the film plane [26]. Having identified one resonance magnetic field (*rf* frequency) at a given stimulus *rf* frequency (magnetic field), one can reasonably estimate as to what range of magnetic field (frequency) a subsequent FMR will be identified under a different frequency (magnetic field). As accurate estimation of material properties using broadband FMR requires a sequence of these observed resonance fields (frequencies) to evaluate the film properties, an experimenter may use this knowledge to narrow the range of examined fields (frequencies) around the FMR condition for each subsequent frequency (magnetic field). This approach clearly accelerates the acquisition of FMR data over alternatives that would survey a broader range of frequency (magnetic field). At the same time, this constitutes a model- and not data-dependent acquisition scheme. And as the data itself is likely to better guide where high SNR measurements can be made, alternative approaches should be explored for selecting measurement ranges to deliver better SNR and speed for FMR investigations.

Bayesian experimental design interprets observations based on Bayesian inference and appropriately selects the values of control variables (*e.g.*, the applied fields or frequencies for FMR) to decrease the uncertainties of measured parameters [27]. Recently, optimal Bayesian design was used to speed up the optical detection of magnetic resonance of nitrogen-vacancy centers and achieved more than one order of magnitude acceleration [28]. In this work, we implement optimal Bayesian experiment design [1] in a field-differential VNA-FMR measurement setup. This approach seeks to maximize the FMR measurement time acquiring data points that most effectively sample from the FMR absorption line shape. A systematic comparison between conventional measurement and optimal Bayesian experimental design reveals improvements in SNR and acquisition time that offer uncomplicated implementation and execution in a conventional FMR measurement system.

## II. SETUP AND MEASUREMENT PROCEDURE

As demonstrated in FIG. 1, an FMR spectrometer that combines a two-port, 20-GHz vector network analyzer, a 150-mm-diameter dipole electromagnet, a pair of 100-mm-diameter Helmholtz coils, and a custom-built grounded coplanar waveguide (CPW) board was used in this study. Independent power supply units operating in

current mode were used to excite the dipole electromagnet and the Helmholtz coils, respectively. Experiments were launched using a custom user interface developed in Python and optimal Bayesian design of frequency ranges was carried out using the *optbayesexpt* package developed at the National Institute of Standards and Technology (NIST) [1,29]. An intermediate frequency bandwidth (IFBW) of 100 Hz was chosen for our measurement apparatus but a broader or narrower bandwidth may prove advantageous for white noise rejection in other measurement environments.

A $Fe_{80}B_{20}$ (FeB) sample was tested in this study. The sample was grown by direct current magnetron sputtering in a 14-target custom, ultrahigh vacuum sputter deposition facility (base pressure less than $3 \times 10^{-8}$ Pa). The stack structure of Ta(3)/FeB(20)/Ta(3) was produced on a Si(100) wafer coated with a 500-nm layer of thermal oxide (numbers in parentheses denote thicknesses in nm). All layers were deposited at an ambient temperature of 293 K and under a working Ar pressure of 0.4 Pa with a target-to-substrate distance of 20 cm in a confocal geometry. The sputtering power was 5.3 W/cm$^2$ for the Ta cathode and 4.0 W/cm$^2$ for FeB, leading to a deposition rate of 0.034 nm/s for Ta and 0.025 nm/s for FeB. A small (0.5 cm × 0.5 cm) cleave from a larger (2.0 cm × 2.0 cm) sample was reserved for FMR observations, placed film-side down on the CPW, and placed directly above approximately 2 mm of track length of the 1.1 mm wide center conductor. Conventionally, FMR measurements are conducted under either a field-swept mode or a frequency-swept mode. For the field-swept (frequency-swept) mode, the data are collected with external fields (frequencies of driving electromagnetic waves) fixed and a quasistatic sweep of the microwave frequency (external magnetic field) employing a uniform step size between the endpoints of the sweep range. For the optimal Bayesian design, the swept range is updated after each sweep to maximize the expected information gain for the upcoming measurement. In this work, we present an implementation of the optimal Bayesian experiment design in the frequency-swept mode VNA-FMR to evaluate performance gains over the conventional frequency-swept mode. The field-differential scheme [25] is used to suppress frequency-dependent background signals for both the conventional and the optimal Bayesian measurements. Although the comparison is made under the frequency-swept mode VNA-FMR, the results can be generalized to field-swept mode VNA-FMR and other types of FMR without VNA as well. To evaluate the generalizability of the Bayesian approach in enhancing FMR efficiency, we extended our investigation to a field-swept FMR setup, which has a dedicated microwave generator and a diode detector. A FePd sample with perpendicular magnetic anisotropy was tested. We observed significant improvement in measurement efficiency when the Bayesian approach was implemented (see more details in the Supplementary Materials).

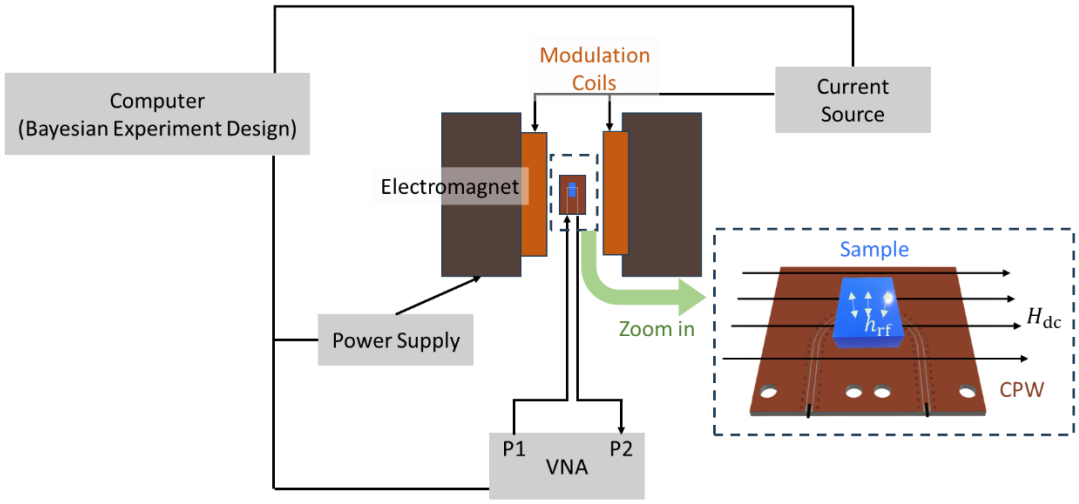


FIG. 1. A schematic of the field-differential VNA-FMR setup used in this study. $H_{dc}$: static magnetic field generated by the electromagnet. $h_{rf}$: radio-frequency magnetic field.

### A. Conventional Measurement Procedure

We highlight the conventional measurement scheme in FIG. 2(a), whereby a linear frequency sweep is repeated several times for white noise reduction and correspondingly to reduce the uncertainties in parameters (resonance field $f_{res}$ and linewidth $\Delta f$) fitted by the least-squares method. For the representative case in FIG. 2(a), each sweep contains 401 evenly distributed frequencies, ranging from 16.19 GHz to 19.19 GHz. In practice, each frequency-swept scan includes two sequential scans with an applied positive/negative field bias (field-differential detection) of 0.5 mT superposed on the background field for each scan (0.200 T, in this case). The magnitude of the bias field is chosen to avoid exceeding approximately 25 % of the linewidth in the field (>~4 mT for the tested sample and frequency range) to avoid possible line shape distortion [25]. Data from the two sequential scans are processed to obtain a field-derivative scattering parameter ($S'_{21}$) from each field-differential sweep [25]:

$$S'_{21}(f) = 2\frac{S^{+}_{21}(f)-S^{-}_{21}(f)}{[S^{+}_{21}(f)+S^{-}_{21}(f)]}, \quad (1)$$

where, $S^{+}_{21}(f)$ and $S^{-}_{21}(f)$ are the scattering parameters from VNA sweeps with a positive and negative bias field, respectively. At the end of the measurements, $S'_{21}(f)$ from the sequential field-differential frequency sweeps [10 sweeps for the case of FIG. 2(a)] are averaged to generate the data used to estimate the resonance frequency and resonance linewidth.

The real and imaginary parts of the complex transmission parameter $S'_{21}(f)$ reflect the derivative of the absorptive and dispersive effects of the magnetic thin film altering the inductance of the CPW. They can be fitted by the derivative Lorentzian function [30,31]:

$$S'_{21}(f) = \frac{A_{\text{abs}}\Delta f(f-f_{\text{res}})}{\left[(f-f_{\text{res}})^2+\left(\frac{\Delta f}{2}\right)^2\right]^2} + i\frac{A_{\text{disp}}\left[\left(\frac{\Delta f}{2}\right)^2-(f-f_{\text{res}})^2\right]}{\left[(f-f_{\text{res}})^2+\left(\frac{\Delta f}{2}\right)^2\right]^2}, \quad (2)$$

where $A_{\text{abs}}$, $A_{\text{disp}}$, $f_{\text{res}}$, and $\Delta f$ are the amplitudes of absorptive and dispersive terms, resonance frequency, and line width, respectively. Unless stated otherwise, only the real part of $S'_{21}$ is used to fit the absorptive term for $f_{\text{res}}$ and $\Delta f$ after observing a stronger phase noise contribution to the imaginary component $\text{Im}(S'_{21})$ in our particular experimental apparatus. Figure 2(b) shows the real part of $S'_{21}$ obtained by averaging 10 field-differential sweeps. For each sweep, 401 data points are evenly distributed in the swept frequency range. The least-squares fitting yields $f_{\text{res}} = (17.5004 \pm 0.0036)$ GHz and $\Delta f = (0.3469 \pm 0.0143)$ GHz where the reported error bars represent the one-sigma fitting error associated with the best-fit parameters.

Each 401-frequency VNA scan (using a 100-Hz IFBW) requires 3.95 s of sweep time, with an additional 0.35 s for setting the alternating bias fields, plus some additional overhead time to initialize the next sweep and data acquisition. As a consequence, the entire measurement (10 field-differential sweeps) portrayed in FIG. 2(a,b) takes ≈ 87 s. The modulation frequency in this case is 0.12 Hz, much lower than the 5.6 Hz in the previously reported field-differential work [25]. It is mainly caused by the larger number of frequencies (401 *vs.* 53) per sweep and a narrower IFBW (100 Hz *vs.* 1000 Hz) that was picked to balance the suppression of white noise and pink noise in order to optimize SNR with a given measurement duration in our apparatus.

### B. Optimal Bayesian Experimental Design

The optimal Bayesian experimental procedure has two major differences from the conventional mode. Firstly, in addition to the least-squares fitting for $f_{\text{res}}$ and $\Delta f$ at the end of measurements, the optimal Bayesian mode analyzes newly measured $S'_{21}(f)$ after each field-differential sweep to update a probability distribution function (PDF) $p(\boldsymbol{\theta})$ in the fitting parameter space $\boldsymbol{\theta} = (f_{\text{res}}, \Delta f, A_{\text{abs}}, A_{\text{disp}}, \sigma)$, where $\sigma$ denotes the standard deviation of the signal noise. The PDF is updated by using Bayesian inference [28,29]:

$$p_{\text{post}}(\boldsymbol{\theta}) = p[\boldsymbol{\theta}|S'_{21}(f)] = p[S'_{21}(f)|\boldsymbol{\theta}] \cdot p_{\text{prior}}(\boldsymbol{\theta})/p[S'_{21}(f)], \quad (3)$$

where the prior $p_{\text{prior}}$ and the posterior $p_{\text{post}}$ are the PDF updated after the last sweep and the current sweep. The initial prior PDF is obtained by conducting least-squares fitting on $S'_{21}(f)$ of the first sweep, as detailed later. $p[S'_{21}(f)]$ in the denominator is assumed to be a constant.

Secondly, before each field-differential sweep, the up-to-date $p$ is used to calculate the utility of different sweep settings. Utility estimates the benefit (in terms of lowering the variance of the parameter distribution) per

unit of measurement duration. When the allowable measurement settings are a serial of discrete frequencies, the utility of a sweep that covers a set of frequencies $\{f_i\}$ can be defined as [28,29]:

$$U(\{f_i\}) = \frac{1}{T}\sum_i \sigma^2_{S'_{21},\boldsymbol{\theta}}(f_i)/\sigma^2_{S'_{21}}(f_i) \ . \tag{4}$$

$\sigma_{S'_{21},\boldsymbol{\theta}}(f_i)$ and $\sigma_{S'_{21}}(f_i)$ are the variance of signal at measured frequency $f_i$ caused by the probability distribution of $\boldsymbol{\theta}$ and noise. Intuitively, a large $\sigma^2_{S'_{21},\boldsymbol{\theta}}(f_i)/\sigma^2_{S'_{21}}(f_i)$ indicates the signal at $f_i$ is relatively more sensitive to the fitted parameters ($f_{\mathrm{res}}, \Delta f, ...$) than to noise. Therefore, $\sigma^2_{S'_{21},\boldsymbol{\theta}}(f_i)/\sigma^2_{S'_{21}}(f_i)$ serves as a good indicator for the benefit of a sweep. On the other hand, the measurement duration of the sweep $T = T_{\mathrm{s}} + N_{\mathrm{freq}}T_0$, represents the cost. $T_{\mathrm{s}}$ and $T_0$ are the additional time needed for starting a new sweep and the sweep time at individual frequencies. $N_{\mathrm{freq}}$ is the number of frequencies per sweep. With a discrete allowable frequency set, the Bayesian design returns both the optimal number and range of frequencies for the next sweep. In general, when $T_{\mathrm{s}}/T_0$ is larger, the optimized sweep has a larger number of frequencies that span a wider range around the frequency with the highest benefits. However, in VNA-FMR, there are only limited options for the number of frequencies per sweep (*e.g.*, 101, 201, 401, etc.). Therefore, in our measurements, only the frequency range is optimized ($T_{\mathrm{s}}/T_0$ is set as 68). The optimized frequency range, which spans around the most sensitive frequency, is supposed to improve the information yield rate compared to the conventional mode with a fixed frequency range.

In FIG. 2(c), the frequency sequence of optimal Bayesian measurement is illustrated. The first field-differential sweep in the optimal Bayesian mode is the same as the conventional one, where the 401 evenly distributed frequencies are swept through the desired frequency range. Then, the $S'_{21}(f)$ from the first field-differential sweep is fitted with the derivative Lorentzian function to get the best fits ($f^0_{\mathrm{res}}, \Delta f^0$, …) and their uncertainties ( $\sigma_{f^0_{\mathrm{res}}}, \sigma_{\Delta f^0}$ , ... ), which are used to construct the prior $p(f_{\mathrm{res}}, \Delta f, ...) = [N(f^0_{\mathrm{res}}, \sigma_{f^0_{\mathrm{res}}})N(\Delta f^0, \sigma_{\Delta f^0}) ...]$ for the subsequent Bayesian inference. Here, $N(\mu_0, \sigma)$ represents a normal distribution with a mean of $\mu_0$ and a standard deviation of $\sigma$. Starting from the second field-differential sweep, the frequency range is given based on the principle of maximizing utility and each sweep contains 101 frequencies (with a smaller number of frequencies per sweep, the modulation frequency increases to 0.26 Hz). As a result, the frequency range of each subsequent field-differential sweep changes dynamically. In practice, the subsequent sweeps become concentrated in a narrower field range (17 GHz to 18 GHz) around the position of the resonance. In FIG. 2(d), which shows the data collected within 87 s, it can be seen that the resonance region (17.25 GHz to 17.9 GHz) has a much higher data density compared to the region away from the resonance. Consistent with the

utility-maximizing principle, our data imply that more time has been spent measuring in the vicinity of the resonance instead of in the vicinity of the background. The least-squares fit to the Lorentzian expression gives $f_{\mathrm{res}} = (17.5078 \pm 0.0015)$ GHz and $\Delta f = (0.3420 \pm 0.0098)$ GHz (error bars are one-sigma errors of best-fit parameters), reflecting a reduction in the best-fit uncertainty.

Figure 2(e,f) shows the evolution of the one-sigma errors from the least-squares fitting of $f_{\mathrm{res}}$ and $\Delta f$ with measurement duration for both the conventional (401 frequencies per sweep) and the optimal Bayesian mode (101 frequencies per sweep). An examination of the choice of frequencies per sweep, leading to the optimized quantity mentioned above, will be described in a subsequent section. For both measurement design approaches, the uncertainty decreases with measurement duration. When $t > 200$ s, estimated uncertainty approximately follows the $1/\sqrt{t}$ trend and advantageously, the Bayesian approach reduces $\sigma_{f_{\mathrm{res}}}$ by ≈ 60 % and $\sigma_{\Delta f}$ by 40 % compared to the conventional mode. When $t$ is short (< 30 s), both approaches yield similar magnitudes of uncertainty, a consequence of the optimal Bayesian mode initializing with the same first field-differential sweep as the conventional one. For a field-differential sweep of 101 frequencies, it takes the Bayesian mode an extra 0.2 s for Bayesian inference and calculating the subsequent frequency range. Ultimately, the optimal Bayesian mode catches up to the conventional technique and outperforms for measurement durations in excess of 30 s.

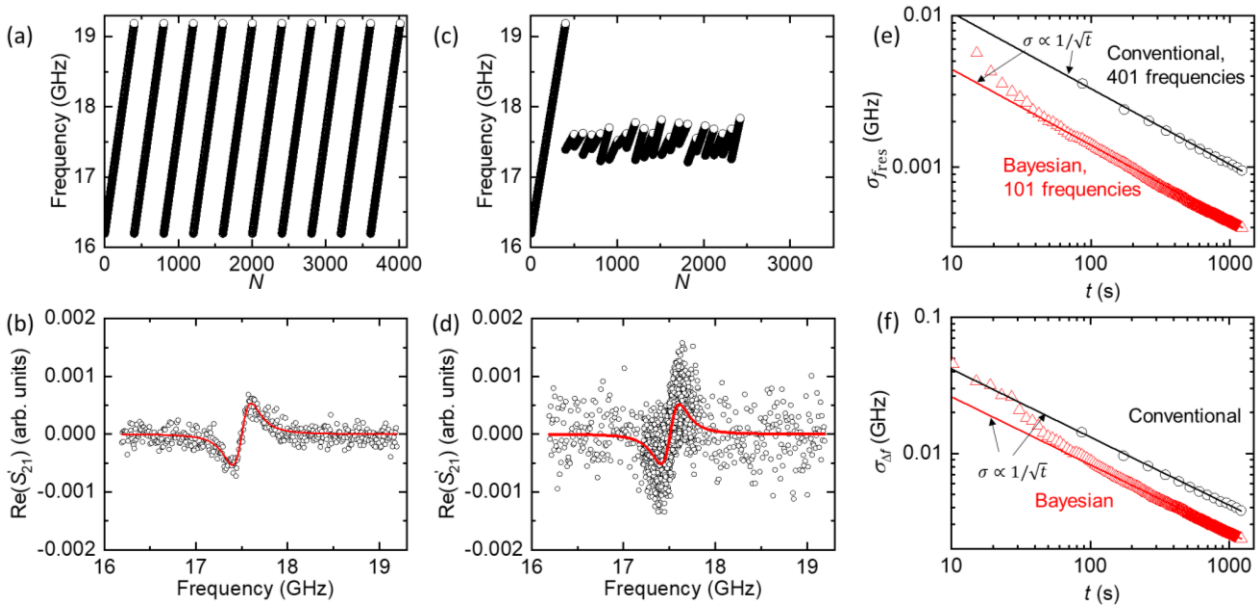


FIG. 2. A comparison of the conventional and the optimal Bayesian experimental procedure. An in-plane external field $\mu_0 H_{\mathrm{ext}}$ =0.2 T is applied. (a,c) The sequence of swept frequencies for (a) the conventional mode and (c) the optimal Bayesian mode. *N* represents the index of frequencies swept in a measurement. (b,d) The real part of the signals (circles) and fits (lines) measured by (b) the conventional mode and (d) the optimal Bayesian mode with a measurement duration of 87 s. The data in (b) represent the averaged results from 10 field-differential sweeps, whereas the data in (d) are unaveraged results from individual field-differential sweeps. (e,f) One-sigma fitting uncertainties of (e) $f_{\mathrm{res}}$ and (f) $\Delta f$ from least squares fitting as a function of measurement duration. Symbols and lines are experimental data and $1/\sqrt{t}$ guidelines, respectively. Black circles and red triangles correspond to conventional and optimal Bayesian experimental designs.

## III. RESULTS AND DISCUSSION

To further compare the two approaches under a typical FMR measurement session of extracting a series of resonance spectra to estimate $\mu_0 M_{\text{eff}}$ and $\alpha$, we evaluated the FMR response of the FeB sample under a series of external magnetic fields ranging from 0.07 T to 0.24 T with an interval of 0.005 T. A measurement duration of 120 s was spent at each applied field. Figure 3 shows the field-dependent $f_{\text{res}}$ and $\Delta f$ measured using both modes. The $f_{\text{res}}$ *vs.* $\mu_0 H_{\text{ext}}$ dispersion relationship is modeled by the Kittel equation for the resonance relationship of a thin film in a planar applied external magnetic field: $f_{\text{res}} = g\mu_{\text{B}}\mu_0/h\sqrt{H_{\text{ext}}(H_{\text{ext}} + M_{\text{eff}})}$, with the Bohr magneton $\mu_{\text{B}} = 9.274 \times 10^{-24}$ J/T and the Planck constant $h = 6.626 \times 10^{-34}$ J ·s. For the conventional mode, the least-squares fitting gives $g = 2.178 \pm 0.007$ and $\mu_0 M_{\text{eff}} = (1.431 \pm 0.011)$ T, where error bars reflect the one-sigma fitting uncertainties. The standard deviation of measured data from the fitting curve $\sigma_{f_{\text{res}},\text{tt}} = 0.009$ GHz, which will be referred to as the total uncertainty in the upcoming discussion. For the optimal Bayesian mode, the least-squares fitting parameters with one-sigma fitting uncertainties are $g = 2.148 \pm 0.006$, $\mu_0 M_{\text{eff}} = (1.479 \pm 0.009)$ T, and $\sigma_{f_{\text{res}},\text{tt}} = 0.0071$ GHz. In FIG. 3, the field dependence of linewidth is fitted by $\Delta f = \partial f/\partial(\mu_0 H_{\text{ext}})\left(\frac{2h}{g\mu_{\text{B}}} f\alpha + \mu_0 \Delta H_0\right)$. For the conventional mode, the least-squares fitting parameters and one-sigma fitting uncertainties are $\alpha = 0.00565 \pm 0.00012$, $\mu_0 \Delta H_0 = (0.027 \pm 0.011)$ mT, and $\sigma_{\Delta f,\text{tt}} = 0.007$ GHz. As for the optimal Bayesian mode, $\alpha = 0.00544 \pm 0.00008$, $\mu_0 \Delta H_0 = (0.044 \pm 0.008)$ mT, and $\sigma_{\Delta f,\text{tt}} = 0.005$ GHz. In short, the optimal Bayesian measurement diminishes the total uncertainty ($\sigma_{\text{tt}}$) in $f_{\text{res}}$ by 21 % and in $\Delta f$ by 29 %. The uncertainties of parameters ($\mu_0 M_{\text{eff}}$ and $g$) from $f_{\text{res}}$ *vs.* $\mu_0 H_{\text{ext}}$ fitting decrease by 14 % and 18 %, respectively while the uncertainties of fitted parameters ($\alpha$ and $\mu_0 \Delta H_0$) from $\Delta f$ *vs.* $\mu_0 H_{\text{ext}}$ fitting fall by 27 % and 33 %, respectively. One may notice that the diminished uncertainties of $\mu_0 M_{\text{eff}}$, $g$, $\alpha$, and $\mu_0 \Delta H_0$ (reductions from 14 % to 33 %) are not as large as that in the uncertainties of $f_{\text{res}}$ and $\Delta f$ (60 % and 40 %, respectively). This can be explained by the contribution of systematic errors in addition to the random errors that are reduced by the optimal Bayesian approach. Systematic error causes repeatable deviations of measured values from the true values of $f_{\text{res}}$ or $\Delta f$, which does not diminish with repeating measurements. Within our setup, one apparent source of systematic error arises from the variation of the power level in the transmission line. This contribution could be further minimized by leveling the power of the transmission line across the entire frequency range. Although the fluctuation of $f_{\text{res}}$ or $\Delta f$ repeatedly measured at a given external field is due to random errors, the deviation of field-dependent $f_{\text{res}}$ or $\Delta f$ from fitting curves has origins in both random and systematic errors. To verify this explanation, the systematic error $\sigma_{\text{sys}}$ can be isolated as one of (at least) two contributions to the total measurement

error, $\sigma_{\mathrm{sys}} = \sqrt{\sigma_{\mathrm{tt}}^2 - \sigma_{\mathrm{ran}}^2}$, where $\sigma_{\mathrm{ran}}$ is an estimation of the random error in $f_{\mathrm{res}}$ or $\Delta f$ calculated by the root mean square of one-sigma fitting errors of $f_{\mathrm{res}}$ or $\Delta f$ under a series of fields: $\sigma_{\mathrm{ran}}\sigma_{\mathrm{ran}} = \sqrt{M^{-1}\sum_{i=1}^{M}\sigma_{\mathrm{fit},i}^2}$.. In the expression, $M$ is the number of fields chosen ($M = 35$, from 0.07 T to 0.24 T with a field interval of 0.005 T). For the conventional mode, the estimated systematic error contributions are $\sigma_{f_{\mathrm{res}},\mathrm{sys}} = 0.0089$ GHz and $\sigma_{\Delta f,\mathrm{sys}} = 0.0039$ GHz, while for the optimal Bayesian mode, the systematic errors are $\sigma_{f_{\mathrm{res}},\mathrm{sys}} = 0.0071$ GHz and $\sigma_{\Delta f,\mathrm{sys}} = 0.0029$ GHz. Our results suggest that $\sigma_{f_{\mathrm{res}},\mathrm{tt}}$ is dominated by the systematic error $\sigma_{f_{\mathrm{res}},\mathrm{sys}}$, which explains the limited improvement in $f_{\mathrm{res}}$ fitting brought by the Bayesian mode. However, for $\sigma_{\Delta f,\mathrm{tt}}$, the contribution of systematic error is comparable to that of random error. Therefore, a relatively higher improvement from the Bayesian mode is observed on the $\Delta f$ *vs.* $\mu_0 H_{\mathrm{ext}}$ fitting. The results also imply that if the measurement goal is strictly quantifying the dispersion relationship $f_{\mathrm{res}}$ *vs.* $\mu_0 H_{\mathrm{ext}}$ (without $\Delta f$ *vs.* $\mu_0 H_{\mathrm{ext}}$), short measurement durations [*e.g.,* 20 s, based on FIG. 2(e), which yield $\sigma_{f_{\mathrm{res}},\mathrm{ran}}$ that are comparable to $\sigma_{f_{\mathrm{res}},\mathrm{sys}}$] can be adopted without significantly compromising the uncertainties of the final estimated parameters ($g$ and $M_{\mathrm{eff}}$). With a shorter measurement duration, the random errors increase and become a more important contribution to the total error. In this case, the optimal Bayesian approach, which reduces random errors, may be more effective in reducing the uncertainties of $g$ and $M_{\mathrm{eff}}$.

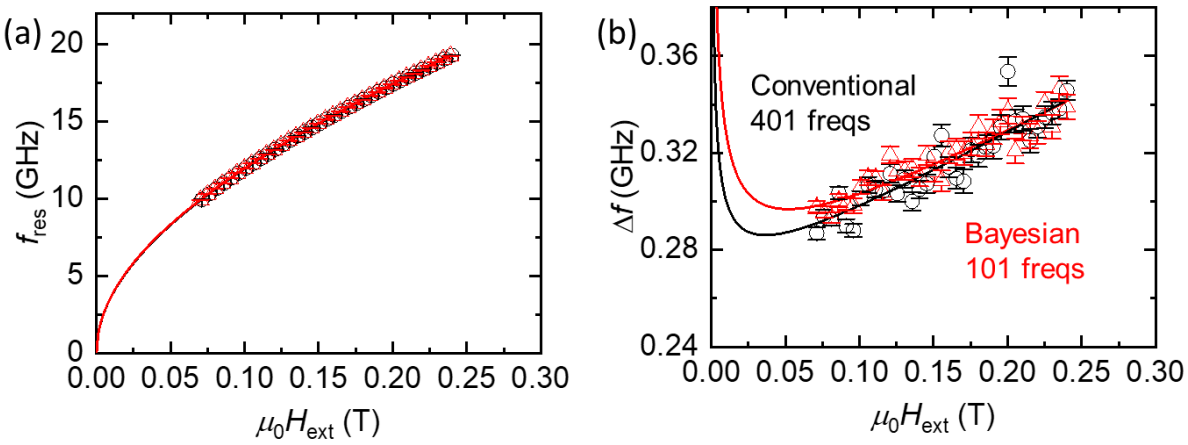


FIG. 3. Field-dependent $f_{\mathrm{res}}$ (a) and $\Delta f$ (b) measured using conventional (black circles) and optimal Bayesian (red triangles) experimental designs. Circles and solid lines represent measured data and fits.

For field-differential VNA-FMR measurements, the choice of $N_{\mathrm{freq}}$ for each sweep directly affects the sweep time and, therefore, the modulation frequency. In general, a larger number of frequencies requires a longer sweep time and results in lower modulation frequency, which makes the signals more vulnerable to pink noise [25]. However, a small number of frequencies has apparent drawbacks as well, leading to a large frequency interval

and, correspondingly, larger discretization error for the resonance frequency and frequency linewidth. Here, we compare the performance of the conventional and optimal Bayesian methods using a variety of number of frequencies per sweep (101, 201, 401, 801). The results are summarized in FIG. 4 and FIG. 5. For the conventional mode, significantly larger uncertainties [shown in FIG. 4(a-d) and FIG. 5] are observed when 101 frequencies (0.03 GHz frequency interval) are used. This can be explained by the large discretization errors stated above. The uncertainties of $\Delta f$ decrease with $N_{\text{freq}}$ and increase again when $N_{\text{freq}}$ is 801 [black symbols in FIG. 4(b)], likely due to the high pink noise contribution associated with the low modulation frequency (0.06 Hz). For the optimal Bayesian mode, the measured frequency ranges keep changing. No matter how many frequencies are measured per sweep, the frequency interval in the resonance region can be rather small [see FIG. 2(e)]. Therefore, discretization errors are less of a concern and the 101-frequency case does not have significantly higher uncertainties for the optimal Bayesian mode. On the contrary, owing to the higher modulation frequency (0.26 Hz), the 101-frequency case has the lowest uncertainty for the optimal Bayesian mode. Therefore, as shown in FIG. 2 and FIG. 3, the 401-frequency and 101-frequency cases are selected for comparison of the conventional mode and the optimal Bayesian mode. In FIG. 4(e,f), the orders of magnitude of the estimated systematic errors are relatively consistent: ≈0.008 GHz for $\sigma_{f_{\text{res}},\text{sys}}$ and ≈0.005 GHz for $\sigma_{\Delta f,\text{sys}}$. This makes sense because the systematic errors should be insensitive to the number of frequencies and measurement methods (conventional or optimal Bayesian). Figure 5 presents the one-sigma uncertainties of final fitting parameters. Similar to the trend in FIG. 4, for the conventional approach, the 801-frequency case yields the lowest uncertainties for $g$-factor and $\mu_0 M_{\text{eff}}$ while the 401-frequency case yields $\alpha$ and $\mu_0 \Delta H_0$ with lowest uncertainties. For the optimal Bayesian mode, the 101-frequency case has the lowest uncertainties for $g$-factor, $\mu_0 M_{\text{eff}}$, $\alpha$, and $\mu_0 \Delta H_0$. If we compare the lowest uncertainties measured by the two approaches, the optimal Bayesian mode yields comparable $\sigma_g$, 10 % lower% lower $\sigma_{\mu_0 M_{\text{eff}}}$, 26 % lower $\sigma_\alpha$, and 26 % lower $\sigma_{\mu_0 \Delta H_0}$. For certain cases, fitting Re($S_{21}'$) with both the absorptive term and the dispersive term could yield a lower uncertainty due to the mixing of real and imaginary signals along the transmission line. When the dispersive term is included in the fitting of Re($S_{21}'$), the best Bayesian case yields 29 % lower $\sigma_g$, 20 % lower $\sigma_\alpha$, 19 % lower $\sigma_\alpha$, and 18 % lower $\sigma_\alpha$ than the best conventional case. As discussed previously, a larger improvement is expected if the measurement duration is reduced from the current duration (120 s) as it will make random errors more dominant compared with systematic errors.

In this work, we compare the uncertainties with a given measurement duration. In practice, a more common scenario is shortening the measurement duration required for achieving certain uncertainties. In this case, the

benefits of implementing optimal Bayesian design can be estimated based on the trend: $\sigma_{\mathrm{ran}} \propto 1/\sqrt{t}$. A 40 % (60 %) reduction in $\sigma_{\mathrm{ran}}$ with a given measurement duration corresponds to a 64 % (84 %) reduction in measurement duration with a given uncertainty target. The Bayesian method provides nearly an order of magnitude increase in measurement throughput.

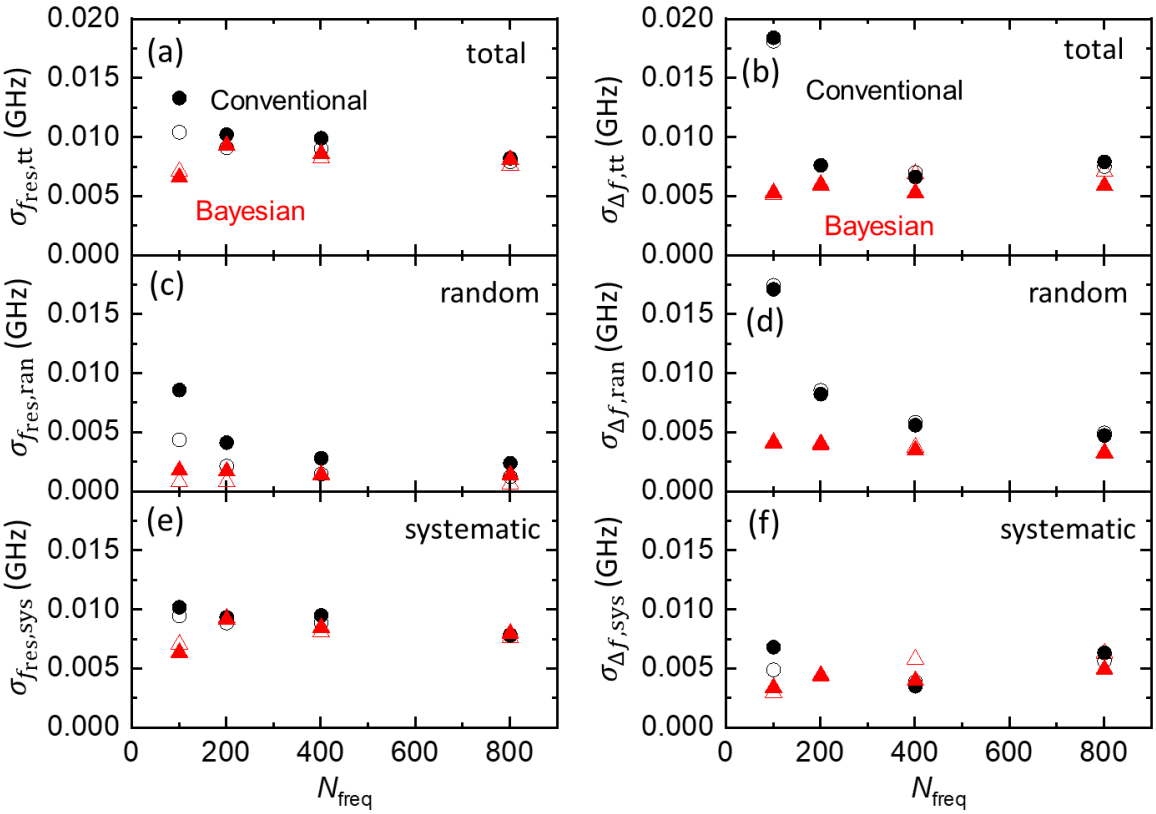


FIG. 4. Impacts of the number of frequencies in each scan ($N_{\mathrm{freq}}$) on the uncertainties of (a,c,e) $f_{\mathrm{res}}$ and (b,d,f) $\Delta f$. (a,b) Total uncertainties calculated by the standard deviation of measurement data from fits. (c,d) Uncertainties from derivative Lorentzian fitting averaged over fields. (e,f) Systematic uncertainties estimated by $\sigma_{\mathrm{sys}}^2 = \sigma_{\mathrm{tt}}^2 - \sigma_{\mathrm{ran}}^2$. Conventional and optimal Bayesian results are denoted by black circles and red triangles, respectively. Solid symbols represent $\mathrm{Re}(S_{21}')$ is fitted by both absorptive and dispersive terms while open symbols are obtained with $\mathrm{Re}(S_{21}')$ fitted by only the absorptive term. For certain cases, fitting with both the absorptive and the dispersive terms generates lower uncertainties possibly due to the mixing of real and imaginary signals.

.

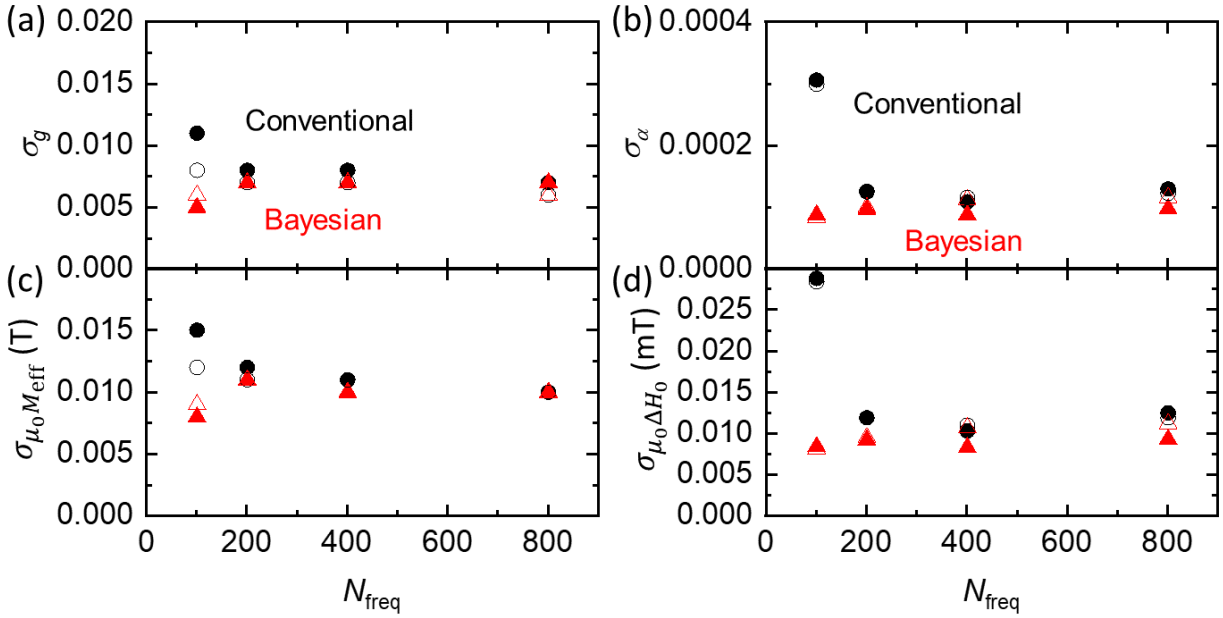


FIG. 5. One-sigma uncertainties of (a) $g$-factor, (b) $\alpha$, (c) $\mu_0 M_{\rm eff}$, and (d) $\mu_0 \Delta H_0$ from fitting. Conventional and optimal Bayesian results are denoted by black circles and red triangles, respectively. Solid symbols represent $\mathrm{Re}(S_{21}')$ is fitted by both the absorptive and the dispersive terms while open symbols are obtained with $\mathrm{Re}(S_{21}')$ fitted by only the absorptive term.

## IX. CONCLUSION

We implemented an optimal Bayesian experimental design in a field-differential VNA-FMR setup. Respective reductions of 60 % and 40 % in the uncertainties of $f_{\rm res}$ and $\Delta f$ were observed with a common measurement time. These reductions are equivalent to 84 % and 64 % decreases in measurement time to achieve the same uncertainty targets as a conventional field-differential VNA-FMR method. The results show that the optimal Bayesian design can significantly accelerate the throughput of FMR measurements. This has particular merit for high-throughput materials screening in research and development environments as well as for fast, wafer-scale quality control in industrial settings, where throughput in FMR techniques could provide particular utility for inspection of 300 mm magnetic memory films.

## ACKNOWLEDGMENTS

D.H. and X.W. acknowledge the funding from the National Science Foundation for supporting D.H.'s internship at NIST (NSF, CBET-2226579). The authors thank Robert D. McMichael, Jenae E. Shoup, and Mark-Alexander Hehn for helpful discussions.

## REFERENCES


[1] R. D. McMichael, S. M. Blakley, and S. Dushenko, Optbayesexpt: Sequential Bayesian experiment design for adaptive measurements, J. Res. Natl. Inst. Stand. Technol. **126**, 126002 (2021).

[2] M. Kief and R. Victora, Materials for heat-assisted magnetic recording, MRS Bull. **43**, 87 (2018).

[3] M. Andreas, T. Kentaro, T. M. David, A. Manfred, S. Yoshiaki, I. Yoshihiro, S. Shouheng, and E. F. Eric, Magnetic recording: Advancing into the future, J. Phys. D: Appl. Phys. **35**, R157 (2002).

[4] A. D. Kent and D. C. Worledge, A new spin on magnetic memories, Nat. Nanotechnol **10**, 187 (2015).

[5] S. S. P. Parkin, M. Hayashi, and L. Thomas, Magnetic domain-wall racetrack memory, Science **320**, 190 (2008).

[6] A. Fert, V. Cros, and J. Sampaio, Skyrmions on the track, Nat. Nanotechnol **8**, 152 (2013).

[7] M. Zabihi, Z. I. Chowdhury, Z. Zhao, U. R. Karpuzcu, J. P. Wang, and S. S. Sapatnekar, In-memory processing on the spintronic CRAM: From hardware design to application mapping, IEEE Trans. Comput. **68**, 1159 (2019).

[8] D. Pinna, G. Bourianoff, and K. Everschor-Sitte, Reservoir computing with random skyrmion textures, Phys. Rev. Appl. **14**, 054020 (2020).

[9] X. Zhu and J. G. Zhu, Effect of damping constant on magnetic switching in spin torque driven perpendicular MRAM, IEEE Trans. Magn. **43**, 2349 (2007).

[10] J. M. Shaw, H. T. Nembach, and T. J. Silva, Resolving the controversy of a possible relationship between perpendicular magnetic anisotropy and the magnetic damping parameter, Appl. Phys. Lett. **105**, 062406 (2014).

[11] J. M. Shaw, R. Knut, A. Armstrong, S. Bhandary, Y. Kvashnin, D. Thonig, E. K. Delczeg-Czirjak, O. Karis, T. J. Silva, E. Weschke *et al.*, Quantifying spin-mixed states in ferromagnets, Phys. Rev. Lett. **127**, 207201 (2021).

[12] M. A. W. Schoen, D. Thonig, M. L. Schneider, T. J. Silva, H. T. Nembach, O. Eriksson, O. Karis, and J. M. Shaw, Ultra-low magnetic damping of a metallic ferromagnet, Nat. Phys. **12**, 839 (2016).

[13] H. J. Waring, Y. Li, N. A. B. Johansson, C. Moutafis, I. J. Vera-Marun, and T. Thomson, Exchange stiffness constant determination using multiple-mode FMR perpendicular standing spin waves, J. Appl. Phys. **133**, 063901 (2023).

[14] M. H. Seavey and P. E. Tannenwald, Direct observation of spin-wave resonance, Phys. Rev. Lett. **1**, 168 (1958).

[15] A. K. Srivastava, M. J. Hurben, M. A. Wittenauer, P. Kabos, C. E. Patton, R. Ramesh, P. C. Dorsey, and D. B. Chrisey, Angle dependence of the ferromagnetic resonance linewidth and two magnon losses in pulsed laser deposited films of yttrium iron garnet, MnZn ferrite, and NiZn ferrite, J. Appl. Phys. **85**, 7838 (1999).

[16] C. T. Boone, J. M. Shaw, H. T. Nembach, and T. J. Silva, Spin-scattering rates in metallic thin films measured by ferromagnetic resonance damping enhanced by spin-pumping, J. Appl. Phys. **117**, 223910 (2015).

[17] J. M. Shaw, H. T. Nembach, T. J. Silva, and C. T. Boone, Precise determination of the spectroscopic g-factor by use of broadband ferromagnetic resonance spectroscopy, J. Appl. Phys. **114**, 243906 (2013).

[18] C. Gonzalez-Fuentes, R. K. Dumas, and C. García, Systematic errors in the determination of the spectroscopic g-factor in broadband ferromagnetic resonance spectroscopy: A proposed solution, J. Appl. Phys. **123**, 023901 (2018).

[19] I. S. Maksymov and M. Kostylev, Broadband stripline ferromagnetic resonance spectroscopy of ferromagnetic films, multilayers and nanostructures, Physica E **69**, 253 (2015).
[20] B. Zhou, P. Khanal, O. J. Benally, D. Lyu, D. B. Gopman, A. Enriquez, A. Habiboglu, K. Warrilow, J.-P. Wang, and W.-G. Wang, Perpendicular magnetic anisotropy, tunneling magnetoresistance and spin-transfer torque effect in magnetic tunnel junctions with Nb layers, Sci. Rep. **13**, 3454 (2023).
[21] D. B. Gopman, C. L. Dennis, R. D. McMichael, X. Hao, Z. Wang, X. Wang, H. Gan, Y. Zhou, J. Zhang, and Y. Huai, Enhanced ferromagnetic resonance linewidth of the free layer in perpendicular magnetic tunnel junctions, AIP Adv. **7**, 055932 (2017).
[22] C. Bilzer, T. Devolder, P. Crozat, C. Chappert, S. Cardoso, and P. P. Freitas, Vector network analyzer ferromagnetic resonance of thin films on coplanar waveguides: Comparison of different evaluation methods, J. Appl. Phys. **101**, 074505 (2007).
[23] J. F. Sierra, A. A. Awad, G. N. Kakazei, F. J. Palomares, and F. G. Aliev, Broadband magnetic response of periodic arrays of FeNi dots, IEEE Trans. Magn. **44**, 3063 (2008).
[24] J. Ding, D. Tripathy, and A. O. Adeyeye, Dynamic response of antidot nanostructures with alternating hole diameters, EPL **98**, 16004 (2012).
[25] S. Tamaru, S. Tsunegi, H. Kubota, and S. Yuasa, Vector network analyzer ferromagnetic resonance spectrometer with field differential detection, Rev. Sci. Instrum. **89**, 053901 (2018).
[26] M. Farle, Ferromagnetic resonance of ultrathin metallic layers, Rep. Prog. Phys. **61**, 755 (1998).
[27] K. Chaloner and I. Verdinelli, Bayesian experimental design: A review, Stat. Sci. **10**, 273 (1995).
[28] S. Dushenko, K. Ambal, and R. D. McMichael, Sequential Bayesian experiment design for optically detected magnetic resonance of nitrogen-vacancy centers, Phys. Rev. Appl. **14**, 054036 (2020).
[29] R. D. McMichael (2022). OptBayesExpt: Optimal Bayesian Experiment Design, https://pages.nist.gov/optbayesexpt/ (Accessed 07-25 2023 2023).
[30] Z. Celinski, K. B. Urquhart, and B. Heinrich, Using ferromagnetic resonance to measure the magnetic moments of ultrathin films, J. Magn. Magn. Mater. **166**, 6 (1997).
[31] L. Montanheiro, B. Ricobom, C. A. Dartora, and M. Bonfim, Real-time FMR Lorentzian visualization through a novel synchronous VNA-FMR measurement apparatus, Rev. Sci. Instrum. **93**, 123905 (2022).